RESEARCH ARTICLE

NANO · MICRO small

www.small-journal.com

NIR-II Orthogonal Fluorescent Ratiometric Nanoprobe for In Situ Bioimaging of Carbon Monoxide

Lichao Guo, Qingyuan Wang, Feng Gao, Ying Liang, Haoyue Ma, Desheng Chen, Yue Zhang, Huangxian Ju,* and Xiaobo Zhang**

Carbon monoxide (CO) functions as a significant endogenous cell signaling molecule and is strongly associated with many physiological and pathological processes. However, conventional fluorescence imaging in the visible and near-infrared (NIR) I regions suffers autofluorescence background and photon scattering, hindering the accurate detection of CO in vivo. In addition, the complexity of physiological environments leads to fluctuating fluorescence emission. To solve these problems, herein, the NIR-II fluorescent nanoprobe NP-Pd for in vivo ratiometric bioimaging of CO is developed. In the presence of CO, NP-Pd exhibits responsive enhancement in absorption at 808 nm, which amplifies the fluorescence signal of down-conversion nanoparticles (DCNP) at 1060 nm under 808 nm excitation, while the fluorescence signal of DCNP at 1525 nm under 980 nm excitation remains unchanged and serves as an internal standard. Through this orthogonally ratiometric fluorescence strategy, accurate CO bioimaging and precise diagnosis of acute liver injury diseases are achieved in the mouse model experiments, providing a novel tool for the in vivo detection of CO-related diseases.

1. Introduction

Carbon monoxide (CO), a colorless and odorless gas, is traditionally considered to be lethal to mammals due to its strong affinity to hemoglobin.[1] In the meantime, CO is one of the most important gaseous signaling molecules involved in numerous physiological activities in biological systems, playing a significant role in various physiological and pathological processes. Recently studies have verified that CO implicates the regulation of various biological functions such as vasodilatation, cytoprotection, antiapoptosis, anti-inflammation.[2] In addition, CO holds considerable therapeutic potential as a drug molecule for diseases such as Alzheimer's disease, hypertension, inflammation, heart failure, and acute liver injury.[3] This evolving understanding of CO's multifaceted roles has attracted unprecedented attention to CO, and with the deepening research of CO in biology and medical science, there is a growing scientific imperative to develop convenient and effective methods for detecting this small gas molecule in living systems to assist studies about its functional mechanisms in certain diseases.[4]

Although numerous quantitative analysis techniques for CO have been developed, such as colorimetric detection,[5] electrochemical analysis[6] and gas chromatography,[7] it is still challenging to achieve real-time tracking of CO in living systems in a non-destructive manner. Compared to these traditional approaches, fluorescent probes offer a noninvasive solution for real-time and in situ monitoring of CO in living systems, and their convenient operation, low cost, and high sensitivity have attracted more and more attention in bioimaging and medical applications.[8]Recent studies have demonstrated the feasibility of various fluorescent probes in CO imaging applications, including red aggregation-induced emission (AIE) fluorescent probes for CO imaging in lipopolysaccharide-induced oxidative stress in mice,[9] cell membrane-anchored fluorophores for monitoring CO release in living cells,[10] and two-photon excited near-infrared fluorescent probe for detecting endogenous CO in zebrafish embryos and live mice.[11] Despite these explorations, the complexity of biological backgrounds and the challenges associated with deep tissue imaging continue to pose significant obstacles to fluorescent analysis of CO in vivo.

To solve this problem, a fluorescence imaging technique in the near-infrared II (NIR-II) (1000–1700 nm) region has been developed and exhibited unique advantages including increased tissue penetration, lower autofluorescence, and improved biocompatibility.[12] Since the first application of NIR-II fluorescence probes was reported,[13] various available materials have been employed as fluorescence probes such as

---

L. Guo, F. Gao, Y. Liang, H. Ma, Y. Zhang
School of Pharmacy
Nanjing University of Chinese Medicine
Nanjing 210023, China
E-mail: zhangyue035@njucm.edu.cn

Q. Wang
Department of General Surgery
Nanjing Drum Tower Hospital
Clinical College of Nanjing Medical University
Nanjing, Jiangsu 210008, China

D. Chen, H. Ju, X. Zhang
State Key Laboratory of Analytical Chemistry for Life Science
School of Chemistry and Chemical Engineering
Nanjing University
Nanjing 210023, China
E-mail: hxju@nju.edu.cn; xhzxb@nju.edu.cn

The ORCID identification number(s) for the author(s) of this article can be found under https://doi.org/10.1002/smll.202405320

DOI: 10.1002/smll.202405320

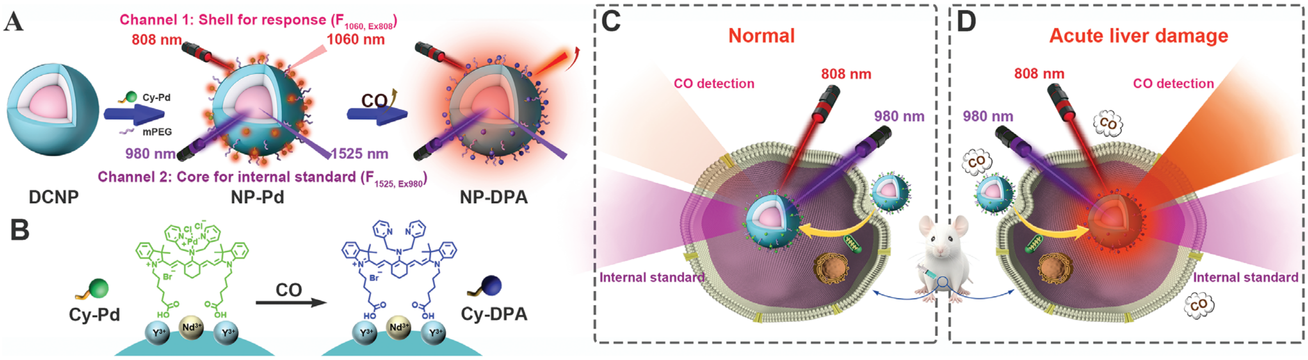

Scheme 1. Schematic Illustration of the imaging mechanism of NIR-II ratio fluorescent nanoprobes for the detection of CO. A) Structural composition of NP-Pd and mechanism of response to CO. B) The corresponding reaction of Cy-Pd with CO. Luminescent applications of NP-Pd in C) normal and D) biological diseases.

single-walled carbon nanotubes,[14] quantum dots (QDs),[15] lanthanide-doped nanoparticles (LnNPs)[16] and small-molecule organic fluorophores.[17] Compared to polymers, QDs, and organic fluorescent molecules, lanthanide-based down-conversion nanoparticles (DCNP) emit NIR-II photons at longer wavelengths by absorbing high-energy photons. In particular, the high quantum yield of Nd^{3+} ions and the emission of Er^{3+} ions at wavelengths in excess of 1500 nm allow for deeper tissue penetration. In addition, traditional fluorescent probes that rely solely on intensity measurements are insufficient for the accurate quantification of intracellular CO due to the effects of excitation fluctuations, sample environment, and local probe concentration on its emission intensity, as well as interference from background fluorescence.[18] In contrast, a ratiometric measurement approach allows for the mitigation of these confounding factors and thus enhances detection accuracy. By utilizing orthogonally designed self-correcting channels, variations in excitation intensity, probe concentration, and sample environment could be effectively compensated.[19]

Herein, we developed a NIR-II orthogonal ratiometric fluorescence nanoprobe for quantitative detection and visualization of CO in vivo, as explicitly depicted in **Scheme** 1A. The nanoprobe was prepared by NIR dye heptamethine cyanine-palladium complex (Cy-Pd) and methoxy-PEG$_4$-COOH (mPEG) on the surface of DCNP, forming CO-responsive nanoprobe (NP-Pd). DCNP as a luminescent body has orthogonally excited NIR-II fluorescence properties and shows emissions at 1060 nm (excited under 808 nm) or 1525 nm (excited under 980 nm). Cy-Pd is modified onto the DCNP surface through strong coordination of carboxyl groups with rare earth ions (Scheme 1B), serving as an absorber of 808-nm irradiation without fluorescence emission due to the heavy atom effect.[20] When NP-Pd is exposed under 808-nm excitation, the strong absorption of Cy-Pd diminishes the energy flux to NP-Pd, which in turn reduces its emission intensity at 1060 nm and achieves a "turn off" fluorescence effect. In the presence of CO, Cy-Pd molecule reacts with CO to form Cy-DPA, which has extremely low absorbance at 808 nm, resulting in the disappearance of energy absorption for irradiation light. Consequently, NP-Pd absorbed additional energy, leading to an enhancement of NIR-II fluorescence emission signal at 1060 nm under 808-nm excitation (recorded as $F_{1060,\ \mathrm{Ex808}}$). By contrast, 980 nm laser is not influenced by Cy-Pd or Cy-DPA molecules, allowing for the direct excitation of DCNP to generate 1525-nm emission (recorded as $F_{1525,\ \mathrm{Ex980}}$), which serves as the reference signal to achieve ratiometric detection of CO. In addition, the presence of mPEG improves the water solubility and biocompatibility of NP-Pd for application in imaging and detection of CO in vivo, which displays enhanced 1060-nm emission and higher ratio values of $F_{1060,\ \mathrm{Ex808}}$ and $F_{1525,\ \mathrm{Ex980}}$ for mice with acute liver damage (Scheme 1C,D). The ratiometric NIR-II fluorescence nanoprobe can accurately quantify and visualize CO in vivo, thus reflecting the state of in situ inflammation. In summary, this NIR-II orthogonal fluorescence imaging system enables the detection of CO not only in vitro but also has the potential for in vivo applications in the diagnosis of CO-related diseases. This work is expected to inspire further innovations in research directions and approaches in the fields of bioimaging and detection.

2. Results and Discussion

2.1. Optimization of DCNP for Orthogonal Emission and the Properties of Cy-Pd

The designed downconversion nanoparticles (DCNP) with core–shell–shell (CSS) architecture ($NaYF_4$:Yb,Er,Ce@$NaYF_4$@$NaYF_4$:Nd) were composed of a downconversion core, inert layer, and downconversion zone (**Figure** 1A). To gain downconversion emissions at 1525 nm, the Yb^{3+} (excited at 980 nm), $Er^{3+,}$ and Ce^{3+} ions were co-doped into the core $NaYF_4$ host lattice. Ce^{3+}-doping modulated the intermediate 4f–4f transitions of Er^{3+}, which increased luminescence at 1525 nm by several times.[21] Subsequently, optically inert $NaYF_4$ was wrapped on the core to isolate the energy transfer between the outer layer and the core. The outer layer $NaYF_4$:Nd^{3+} can absorb 808 nm light and emit NIR-II light 1060 nm, forming orthogonal emission (Figure 1B). The Y^{3+} matrix, with its optically inert properties, functions as an intervening separator to create a distinct boundary between the core (Er^{3+} and Ce^{3+}) and shell (Nd^{3+}) and generate two orthogonal compartments that can be utilized for disparate applications[22] To achieve the effective orthogonal effect, a certain thickness of the inert layer was required for the independent operation of the core and shell components and enabling the realization of orthogonal functionality. We first obtained a batch of core with an average diameter ≈17 nm, and then

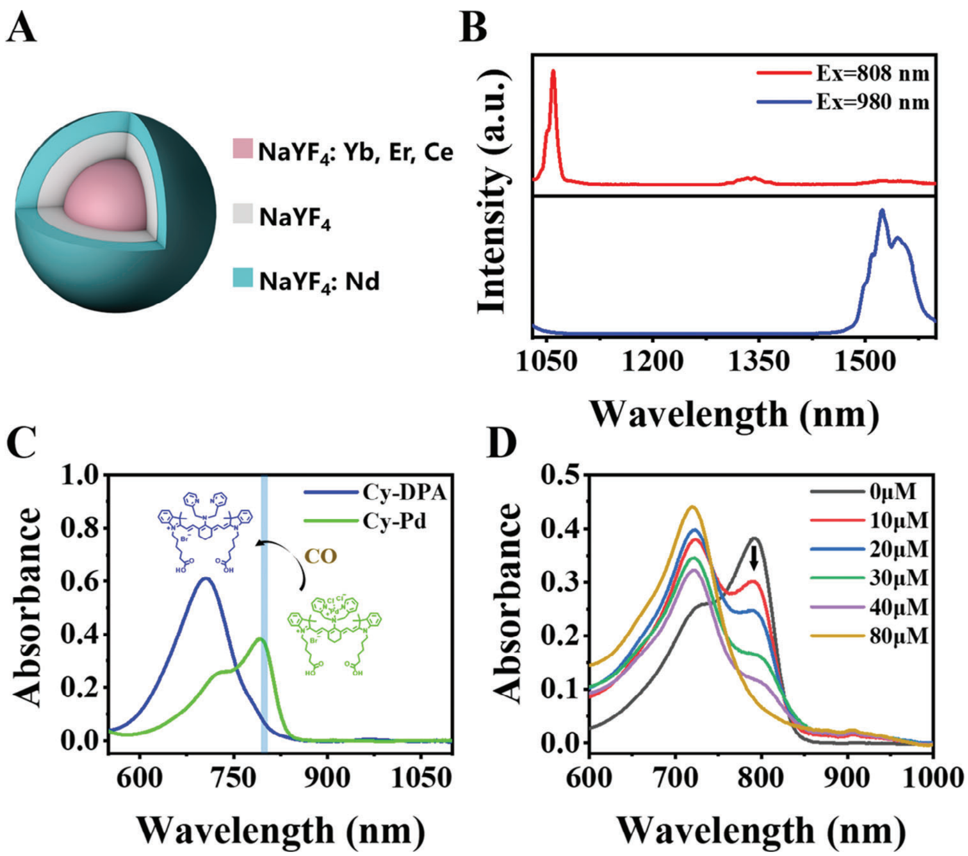

Figure 1. Structure and characterization of DCNP and Cy-Pd. A) Schematic diagram of the core–shell structure of DCNP. B) Luminance spectra of DCNP when exposed to radiation at 808 and 980 nm. C) Structure and absorption spectra changes of Cy-Pd in the presence of CO. D) Absorbance spectra of Cy-Pd (5 μμ) were tested after the addition of CORM-2 (0–80 μμ, in 30 s).

synthesized down-converted nanoparticles with different atomic ratios of core: shell1: shell2 (1: N: 1). As shown in Figure S1 (Supporting Information), the optimal ratio of 1:2:1 was determined by fluorescence spectroscopy in the NIR-II region,[23] and the synthesis of downconversion nanoparticles was carried out with this ratio. Transmission electron microscope (TEM) images confirmed the successful synthesis of NaYF$_4$: 18%Yb, 2%Er, 20%Ce nanocrystal core, NaYF$_4$: 18%Yb, 2%Er, 20%Ce@ NaYF$_4$ and NaYF$_4$: 18%Yb, 2%Er, 20%Ce@ NaYF$_4$@ NaYF$_4$: 5%Nd nanoparticles, with the nanoparticle at each stage of average sizes of 16.5, 22.5, and 26.5 nm, respectively (Figure S2, Supporting Information). Ultimately, our synthesized DCNP exhibited satisfactory orthogonal NIR-II fluorescent properties and displayed distinct emissions at 1060 nm (excited under 808 nm) and 1525 nm (excited under 980 nm) (Figure 1B).

To achieve NIR-II fluorescence responsiveness to CO, we chose heptamethine cyanine-palladium complex (Cy-Pd)[20] as the signal conversion element, Cy-Pd consisted of heptamethine cyanine-dimethylpyridinamine (Cy-DPA) as fluorophore and Pd-contained complexes as recognition unit was designed and synthesized according to the synthetic routes in Figure S3 (Supporting Information), which was characterized by ^{1}H NMR, ^{13}C NMR, and HRMS (Figures S4–S18, Supporting Information). CO is a typical reducing agent and can react with Pd^{2+} quickly and efficiently.[24] After treatment with CORM-2 (as CO releasing agent),[25] the absorption wavelength of the mixture showed a blue shift (peaks from 800 to 710 nm, Figure 1C), indicating the configuration inversion of Cy-Pd to Cy-DPA due to the formation of a complex between Pd^{2+} and CO at room temperature. The quantitative results are shown in Figure 1D. After 30 s of mixing, the absorption peak at 800 nm decreases rapidly and the peak at 710 nm rises rapidly with the gradient increase of CORM-2 concentration. These results establish a fundamental basis for developing quantitative methods of CO, thereby enabling the precise measurement of CO concentrations in various environments.

2.2. Preparation and Properties of the NP-Pd Nanoprobe

CO-responsive NP-Pd nanoprobe was prepared by adding predetermined proportions of Cy-Pd and mPEG to bared DCNP (Figure S19, Supporting Information). Cy-Pd and mPEG were modified on the DCNP surface via coordination. During this process, its average size (based on the dynamic light scattering, DLS) increased from 28.7 to 33.9 nm (**Figure 2A**; Figure S20, Supporting Information). Following conjugation of the dyes onto the DCNP, the zeta potential underwent significant decreases, shifting from +33 mV to +22.3 (NP-DPA) and +29.4 mV (NP-Pd), respectively, which provided evidence for the successful attachment of dyes to the DCNP surface. Furthermore, the smaller decrease

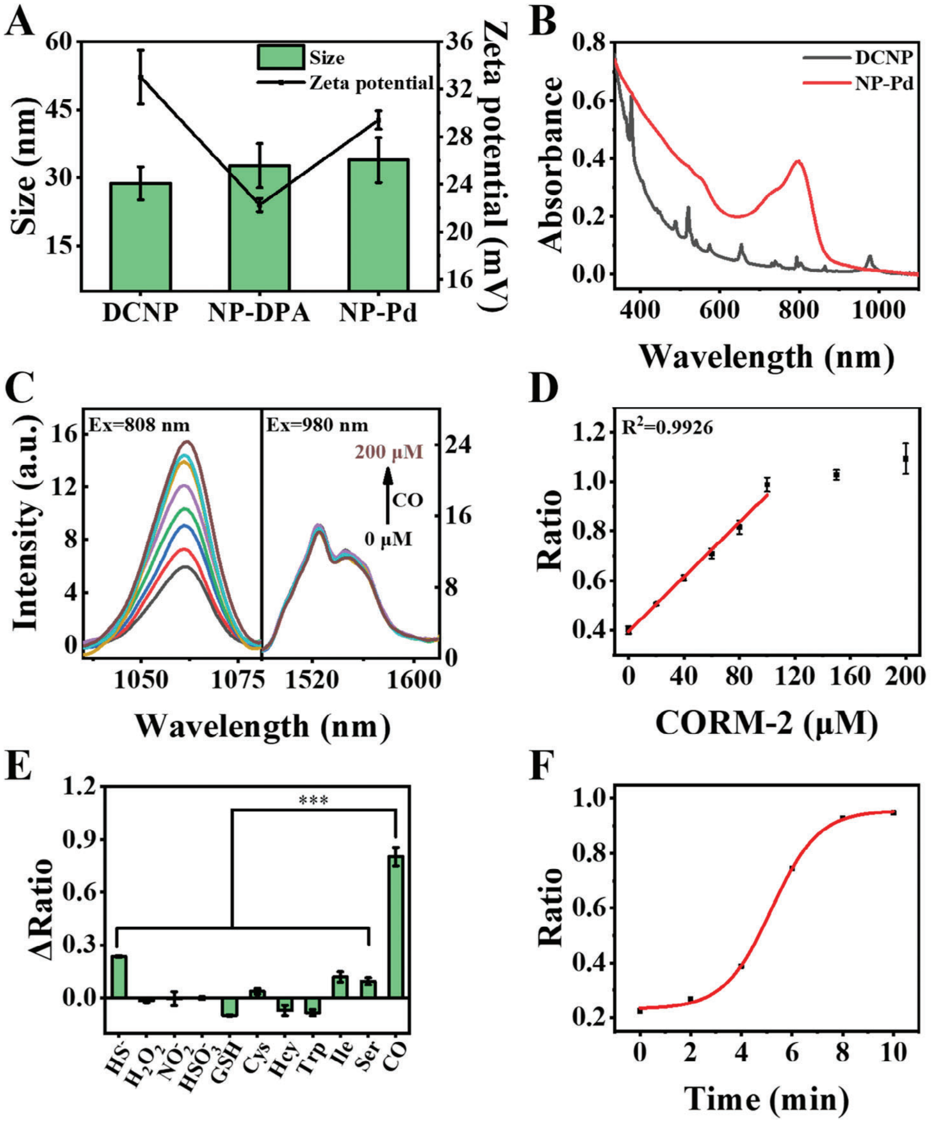

Figure 2. Synthetic characterization and fluorescence response of NP-Pd. A) Particle sizes and zeta potentials of DCNP, NP-DPA and NP-Pd. B) Absorption spectra of DCNP and NP-Pd. C) NIR-II fluorescence spectra of the nanoprobe after reaction with 0–200 μM CORM-2 under 808 and 980 nm laser. D) $F_{1060,\ Ex808}/F_{1525,\ Ex980}$ were linearly related to CORM-2 concentration in the range of 0–100 μM. E) Selectivity of NP-Pd (0.3 mg·mL^{-1}) for CORM-2 (0.1 mM) over various analytes (10 mM) ($n = 3$, mean ± SD). F) Time-dependent fluorescence intensity of NP-Pd (0.3 mg mL^{-1}) after CORM-2 (100 μM) were added. $^{***}p < 0.001$.

in zeta potential for NP-Pd compared to NP-DPA suggested that the incorporation of Pd^{2+} ions mitigated the alteration in surface charge, effectively leading to a reduced variation in zeta potential. In Figure 2B, the absorption (grey line) of DCNP ≈800 nm was itself substantially weak, resulting in a low excitation efficiency of the laser at 808 nm. Meanwhile, due to the Cy-Pd molecules attached on the surface of DCNP, the UV absorption of NP-Pd (red line in Figure 2B) at 808 nm was enhanced by 13 times compared with that of DCNP, and the inner filter effect of Cy-Pd molecules led to a greater reduction of the 808 nm absorption of NP-Pd before responding to CO, and the original fluorescence values of the DCNP, as well as the background signals, were reduced. We further investigated the influence of Cy-Pd loading concentration on DCNP fluorescence. As shown in Figure S21 (Supporting Information), with the increasing reaction concentration of the dye Cy-Pd, the ratio value of 1060-nm fluorescence signal and 1525-nm internal standard intensity ($F_{1060,\ Ex808}/F_{1525,\ Ex980}$) decreased significantly and reached the quenching plateau at 0.1–0.5 mM. Thus, we finally adopted a dye concentration of 0.1 mM for subsequent experiments and concluded the ratio of the amount of DCNP to Cy-Pd is ≈1:191 (Tables S1 and S2, Supporting Information).

Next, we verified the effect of NP-Pd on CO released from CORM-2 under different environmental conditions, and the results showed that the effects of different environmental and physiological factors were weak and the results were stable. (Figure S22, Supporting Information). The effect of other CO donors was again verified (Figure S23, Supporting Information). The response of the NP-Pd nanoprobe to CO was investigated. NP-Pd nanoprobe was applied to react with different concentrations of CORM-2 in range of 0–200 μм. At the end of the reaction, the nanoprobe was irradiated with 808 and 980 nm lasers to obtain the NIR-II fluorescence intensity at 1060 and 1525 nm, correspondingly. The fluorescence signal of the nanoprobe at 1060 nm exhibited an obvious enhancement with increasing CORM-2 concentration upon irradiation with 808 nm laser. This observation could be attributed to the reaction between CO and Cy-Pd, which facilitated the formation of Cy-DPA and effectively mitigated the inner filter effect of 808-nm light absorption. By contrast, the NIR-II fluorescence signal at 1525 nm was basically unchanged after irradiation with 980 nm laser (Figure 2C). Furthermore, the ratiometric NIR-II fluorescence signals showed gradual elevation as the CORM-2 concentration raised, and a linear response of the signal ratio ($F_{1060,\ Ex808}/F_{1525,\ Ex980}$) to CORM-2 concentration could be observed in the range of 0–100 μм (Figure 2D). The limit of detection (LOD) value of CORM-2 was 6.6 μм whose calculation method for LOD was according to the following formula: LOD = $3\delta/K$ (δ: standard deviation of the response, K: the slope of the standard curve). According to the literature, each mole of CORM-2 releases ≈0.7 moles of CO.[26] Based on the above data, the LOD of CO was calculated to be 4.6 μм. This proved the feasibility of a prepared NP-Pd probe to quantitatively detect CO. Furthermore, the nanoprobe exhibited good stability in the cell culture environment (Figure S24, Supporting Information) and photophysical experiment (Figure S25, Supporting Information).

The specificity of the NP-Pd nanoprobe to CO was also studied. After the nanoprobe was treated with 10 mм HS^-, H_2O_2, NO_2^-, HSO_3^-, GSH, Cys, Hey, Trp, Ile, and Ser, respectively, both 1060 and 1525 nm fluorescence signals showed negligible variation (Figure S26, Supporting Information). Additionally, only in the presence of 0.1 mм CORM-2 did the 1060 nm fluorescence signal and ratio of $F_{1060,\ Ex808}/F_{1525,\ Ex980}$ significantly increase (Figure 2E), indicating that the nanoprobe had excellent specific response to CO. Based on the binding mechanism of CO, which displaces the metal to retrieve the original ligand and considering the presence of NO and H_2S in biological systems, we further tested and demonstrated that different metal elements and gas signaling molecules have a weak effect on the detection system (Figure S27, Supporting Information). In order to further study the response speed of NP-Pd molecule and CO, the reaction time (Figure 2F) was further measured, showing that the reaction was fast and could be completed within 10 min.

2.3. Ratiometric NIR-II Fluorescence Nanoprobe for the Detection of CO In Vitro

Prior to in vitro imaging tests, the cytotoxicity of different concentrations of NP-Pd was first assessed using a standard CCK-8 assay. For 4T1 cells, little cell death was observed after treatment with appropriate concentrations of nanoprobes, indicating low toxicity to cancer cells (Figure S28, Supporting Information), and successful entry of the NPs into the cells was verified under confocal microscopy observation (Figure S29, Supporting Information). To evaluate the feasibility of NP-Pd for monitoring CO levels in living cells, we conducted a series of experiments using 4T1 cells as a model system. After incubation with the nanoprobes, 4T1 cells were further treated with different concentrations of CORM-2, a CO-releasing molecule,[25] to obtain NIR-II fluorescence images around the 1060 nm under 808-nm excitation. The results showed successful observation of NIR fluorescence enhancement with increasing concentration of CORM-2 dosage through the CO detection channel (**Figure** 3A,B). Subsequently, 4T1 cells incubated in 24-well plates were used for ratiometric NIR-II fluorescence detection of intracellular CO, and the results showed that the cells exhibited NIR-II fluorescence image intensities of CO detection channel increased dependently with the concentration of CORM-2 (Figure 3C), whereas NIR-II fluorescence image intensities of the internal standard channel were essentially unchanged (Figure 3D). The ratio of $F_{1060,\ Ex808}/F_{1525,\ Ex980}$ also exhibited an obviously rising tendency with increasing CORM-2 concentration (Figure 3E). This result demonstrates the feasibility of ratiometric nanoprobes for the detection of exogenous CO in cells.

As reported in the literature that heme administration stimulates the expression of heme oxygenase and subsequently upregulates endogenous carbon monoxide production,[27] we sought to test the possibility that NP-Pd senses endogenous CO release via hemin treatment. 4T1 cells were preincubated with different concentrations of hemin (0, 30, and 100 μм) before incubation with NP-Pd. Subsequent imaging showed a progressive increase in ratiometric fluorescence with concentration (Figure S30, Supporting Information). Overall, the above findings support the ability of NP-Pd to image endogenous CO fluctuations in living cells via ratiometric fluorescence imaging modalities.

2.4. In Vivo Visualization of Subcutaneous Exogenous CO

In order to demonstrate the feasibility of NP-Pd for CO detection in vivo, we first injected NP-Pd subcutaneously into the back of mice for imaging. The NP-Pd-only group was used as a control, and different concentrations of CORM-2 (30 and 100 μм) were additionally used to investigate the detection effect of NP-Pd for different CO concentrations. The NIR-II fluorescence signals of the detection channel (Ex = 808 nm) and the internal standard channel (Ex = 980 nm) were recorded at different time points, and the experimental areas were circled with red dotted lines (**Figure** 4A). The results showed that the fluorescence values of both channels in the blank group did not change substantially (Figure 4B). For the experimental group, the fluorescence signals of the detection channel became brighter with the increase of CORM-2 concentration and reached the maximum value ≈10 min, while the internal standard channel did not exhibit obvious variation of fluorescence intensities (Figure 4C,D). In the ratiometric plots of the two channels, we can more clearly observe the difference in the detection of NP-Pd response to different concentrations of CO (Figure 4E), and the experimental results remain consistent with those of the in vitro experiments. This again highlights the importance of ratiometric detection in vivo detection, and the internal standard correction of dual-channel detection can well avoid the

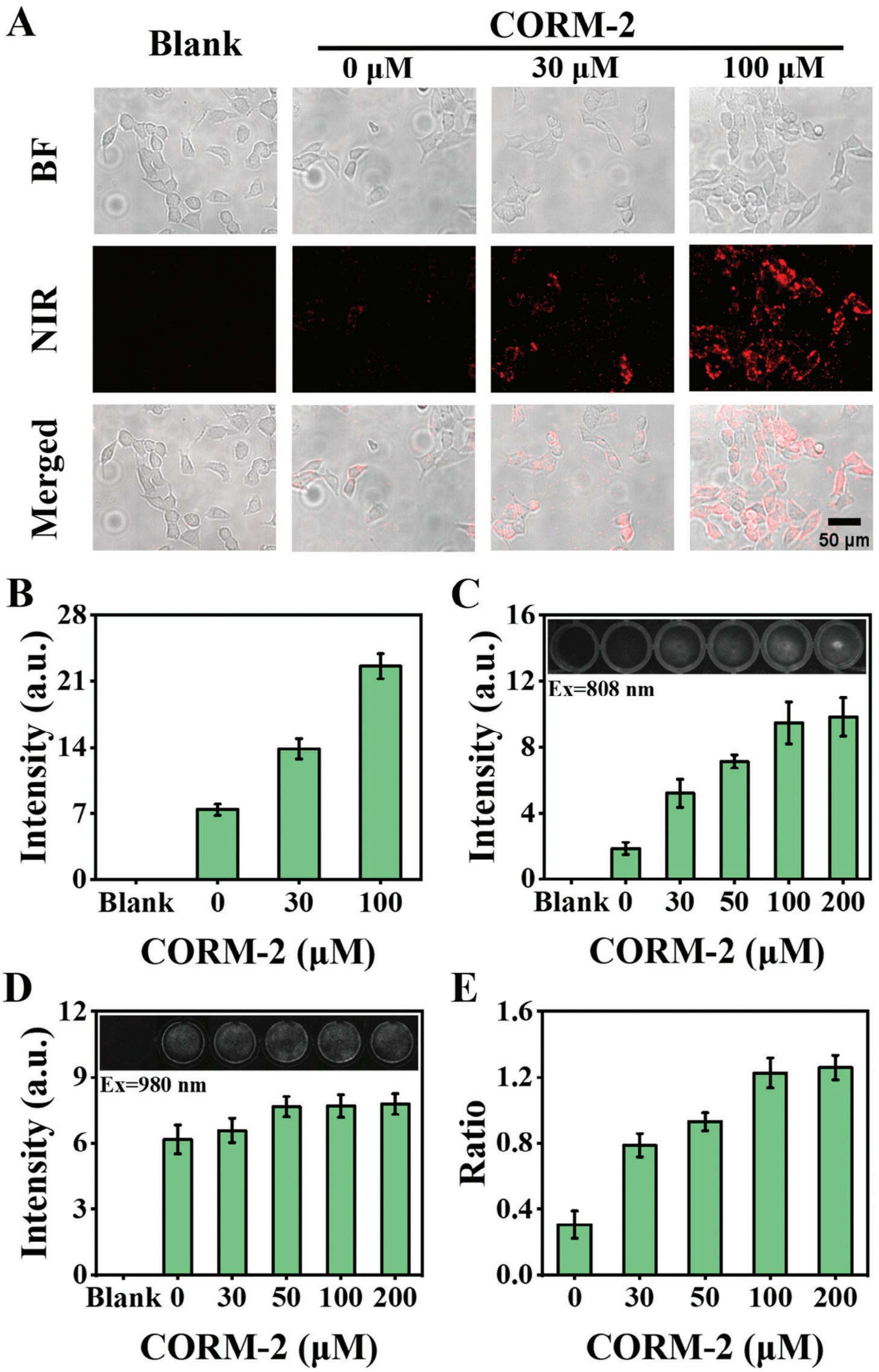

Figure 3. Fluorescence image of NP-Pd in live cells for CO detection. A) Bright field (BF) and NIR-II fluorescence microscopy images and B) corresponding quantitative analyses of 4T1 cells after treatment with no treatment, NP-Pd nanoprobe (0.3 mg mL^{-1}) and different concentrations of CORM-2 (0, 30, and 100 μM) (The excitation wavelength was 808 nm and a 1000 nm long-pass filter (LP 1000) was used). NIR-II fluorescence images of 4T1 cells after treatment with no treatment, NP-Pd nanoprobe (0.3 mg mL^{-1}) and different concentrations of CORM-2 (0, 30, 50, 100, and 200 μM) under C) 808 (LP 1000 was used) and D) 980 nm excitation light (LP 1350 was used). E) Ratio value of $F_{1060,\ Ex808,}$ and $F_{1525,\ Ex980}$ intensities for cells after different treatments in C) and D) ($n = 3$, mean ± SD).

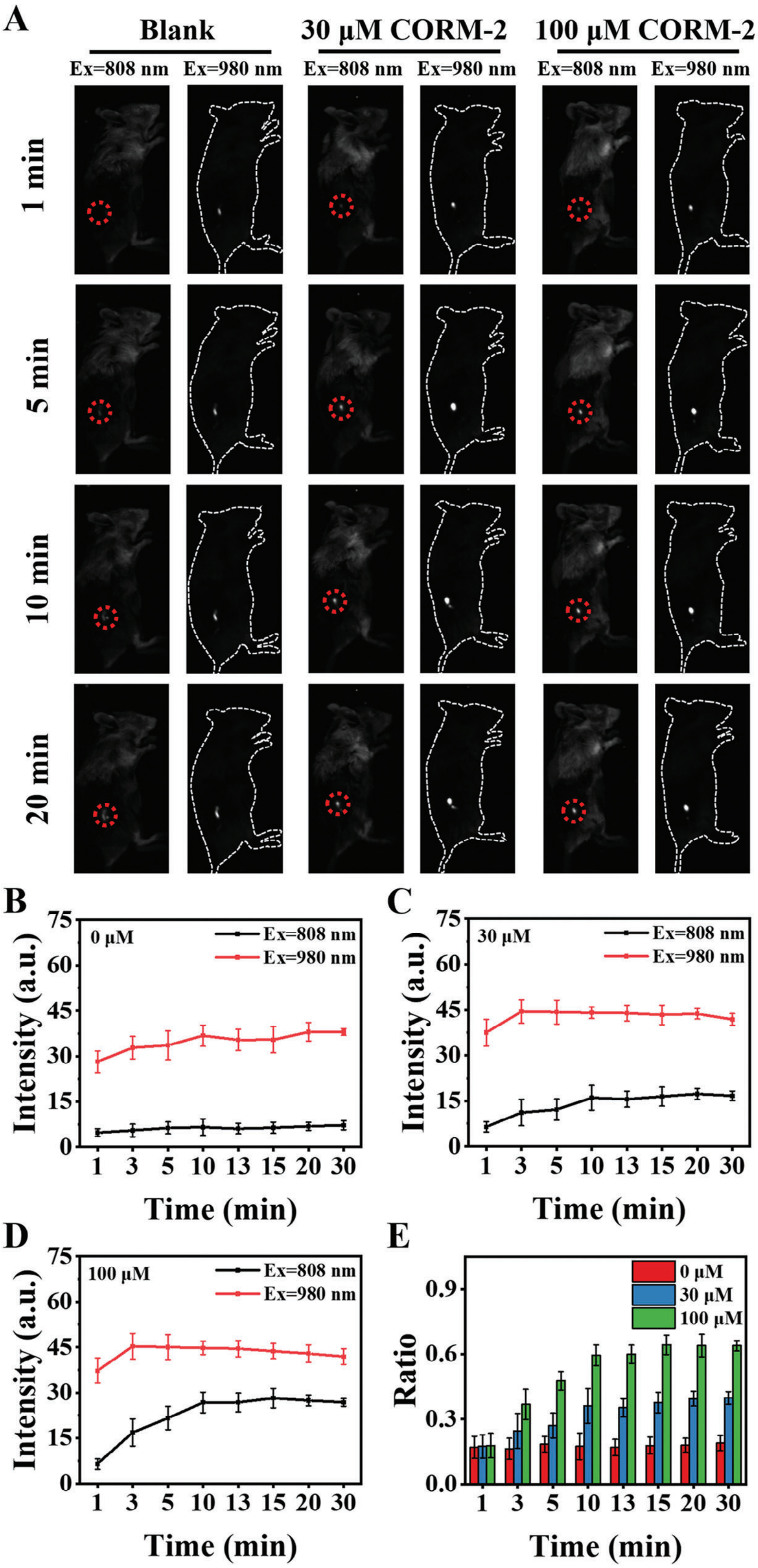

Figure 4. Time-dependent NIR-II fluorescence images of CO in mice. A) NIR-II fluorescence imaging of subcutaneously injected mice treated with NP-Pd and different concentrations of CORM-2 under 808 (LP 1350 was used) or 980 nm laser irradiation (LP 1350 was used). NIR-II $F_{1060,\ Ex808}$ and $F_{1525,\ Ex980}$ intensities at different time points in mice treated with B) 0, C) 30, and D) 100 µM CORM-2 and E) their ratiometric value ($n = 3$, mean ± SD).

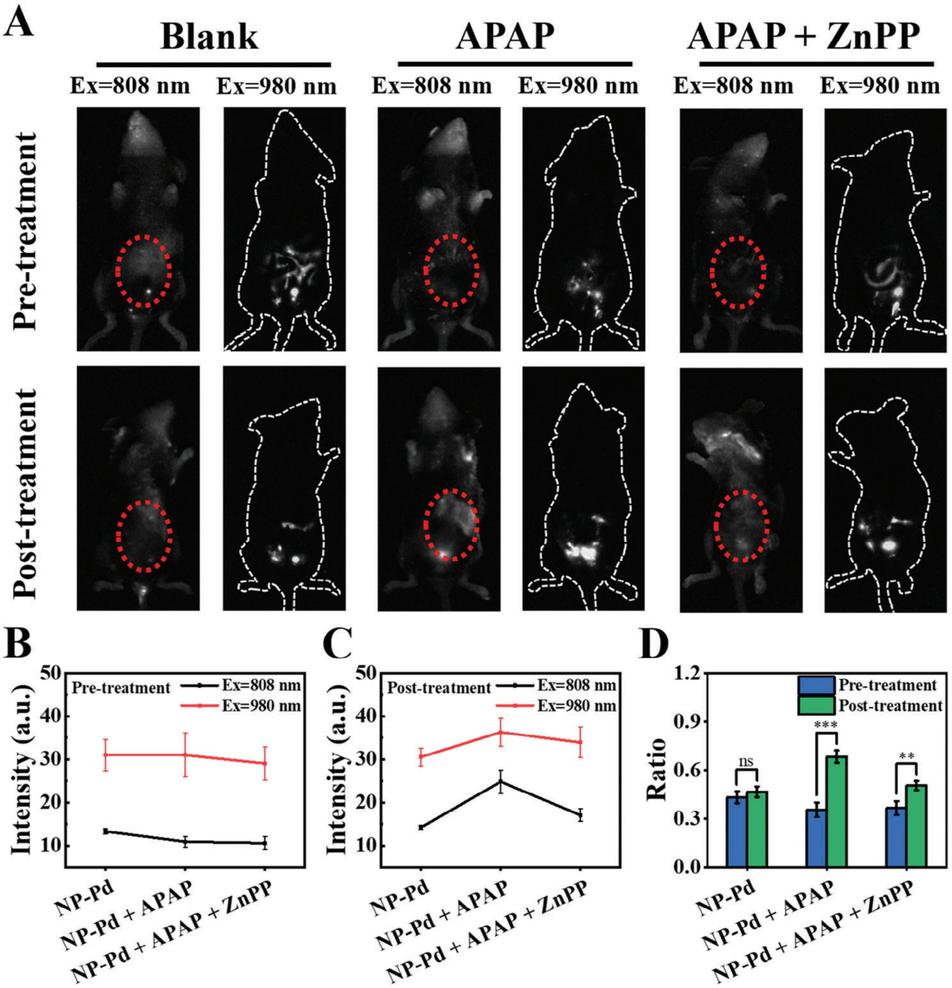

Figure 5. NP-Pd for the detection of CO in mice with acute liver injury. A) NIR-II fluorescence images of live mice that received NP-Pd followed by saline as control, APAP, and APAP + ZnPP, respectively, at the time of injection and 12 h after injection. NIR-II $F_{1060,\ Ex808}$ and $F_{1525,\ Ex980}$ intensities at B) pretreatment and C) post-treatment and D) their ratio value, the probability (P) values in order from left to right are 0.294, 0.000654, 0.00984. ($n = 3$, mean ± SD). $^{**}p < 0.01$, $^{***}p < 0.001$, and ns represents no significant difference.

interference of issues such as drug spreading, injection volume difference, and shooting angle.

2.5. NIR-II Fluorescence Imaging of CO in the Mouse Acute Liver Injury Model

We first investigated the toxicity of the probe in mice. Hematoxylin and Eosin (H&E) staining showed that NP-Pd was weakly invasive to tissues in mice (Figure S31, Supporting Information). It is well known that overuse of N-acetyl-p-aminophenol (APAP) causes severe drug-induced liver injury (DILI) and upregulates CO production.[28] Liver damage was proved by H&E staining (Figure S32, Supporting Information). To further confirm that CO production was indeed induced by APAP, the mice were co-treated with APAP and zinc protoporphyrin (ZnPP), a hemoglobin oxygenase inhibitor that reduces endogenous CO production by inhibiting HO-1 enzyme activity. To evaluate the imaging ability of NP-Pd on CO in vivo, mice were divided into a blank group (NP-Pd only), APAP group, and APAP + ZnPP group.

The mice were injected with the same concentration of NP-Pd in the abdomen followed by injection of different drugs in each group. Their NIR-II fluorescence signals in the detection channel (Ex = 808 nm) and internal standard channel (Ex = 980 nm) were recorded at the time of the first injection of the drug and 12 h after the injection (**Figure 5A**). The experimental areas were circled in red dotted lines. For the internal standard channel, the emission fluorescence intensities at 1525 nm were not significantly changed in all three groups of mice. By contrast, the fluorescence signals of the detected channels in the APAP group increased significantly in comparison with the blank group, whereas the fluorescence signals of the detected channels in the APAP + ZnPP group decreased compared with the APAP group due to the inhibitory effect of ZnPP (Figure 5B,C). The ratiometric fluorescence graphs reflected the experimental results more clearly. The ratiometric fluorescence values in the APAP group showed a significant increase after liver injury compared with those in the blank and APAP + ZnPP group (Figure 5D). The above results indicate that the NP-Pd probe is suitable for the ratiometric optical detection of CO produced during APAP-induced liver injury and as a diagnostic method for DILI.

3. Conclusion

Despite the rapid development and application of fluorescent probes for the detection of CO, there are still many issues to be addressed in the application of bioimaging and in vivo detection.[29] The creation of CO-responsive fluorescent probes with emission in the NIR-II region holds great promise for overcoming the limitations of conventional fluorescent probes, including insufficient biological tissue penetration and spatial resolution, providing a profitable strategy for the study of relevant physiological processes. To achieve quantitative detection and real-time imaging of CO in vivo, we developed a NIR-II ratiometric fluorescent nanoprobe with orthogonal optical properties of 1060-and 1525-nm emissions under 808- and 980-nm excitation respectively. The emission at 1060 nm is affected by the change of the dye's absorption wavelength at 808 nm, achieving a sensitive and specific fluorescent response to CO and serving as a CO detection channel. The ratiometric fluorescence detection was realized by comparison with an internal standard channel which could not be affected by CO. In addition, the ratiometric nanoprobes have demonstrated excellent practicality in detecting CO concentration fluctuations in cellular environments, as well as in monitoring CO levels and diagnosing related diseases in animal models. In conclusion, the designed NP-Pd NIR-II fluorescent nanoprobe presents a valuable platform for investigating CO-related biological processes and provides a novel avenue for the diagnosis and treatment of diseases associated with aberrant CO levels.

Supporting Information

Supporting Information is available from the Wiley Online Library or from the author.

Acknowledgements

The authors gratefully acknowledge the National Natural Science Foundation of China (22004062, 22104063), the National Key R&D Program of China (2023YFC2308200), Natural Science Foundation of Jiangsu Province, China (SBK2021042488), Nanjing University of Chinese Medicine (XPT22104063), and Jiangsu Postgraduate Practice Innovation Project (SJCX23_0851).

Conflict of Interest

The authors declare no conflict of interest.

Data Availability Statement

The data that support the findings of this study are available in the supplementary material of this article.

Keywords

acute liver injury diagnosis, CO detection, near-infrared II, orthogonal excited DCNP, ratiometric imaging

Received: June 28, 2024
Revised: August 14, 2024
Published online:

[1] J. A. Chenoweth, T. E. Albertson, M. R. Greer, *Crit. Care Clin.* **2021**, *37*, 657.

[2] a) R. Motterlini, L. E. Otterbein, *Nat. Rev. Drug Discov.* **2010**, *9*, 728; b) X. Fang, Z. Zhang, Y. Qi, B. Yue, J. Yu, H. Yang, H. Yu, *Anal. Chem.* **2023**, *95*, 11518; c) C. Szabo, *Nat. Rev. Drug Discov.* **2016**, *15*, 185.

[3] a) S. J. Li, D. Y. Zhou, Y. F. Li, B. Yang, J. Ou-Yang, J. Jie, J. Liu, C. Y. Li, *Talanta* **2018**, *188*, 691; b) G. Q. Fu, Y. S. Xia, W. L. Jiang, W. X. Wang, Z. K. Tan, K. Y. Guo, G. J. Mao, C. Y. Li, *Talanta* **2022**, *243*, 123398; c) L. Liu, J. Xu, S. Zhang, H. Chen, L. Wang, X. C. Shen, H. Chen, *Sens. Actuator B-Chem.* **2022**, *367*, 132171.

[4] a) S. Feng, D. Liu, W. Feng, G. Feng, *Anal. Chem.* **2017**, *89*, 3754; b) L. Yan, C. Zhou, H. Yang, *Sens. Actuator B-Chem.* **2023**, *382*, 133492.

[5] W. Duan, J. Wang, X. Peng, S. Cao, J. Shang, Z. Qiu, X. Lu, J. Zeng, *Biosens. Bioelectron.* **2023**, *223*, 115022.

[6] K. Sonda, T. Kodama, M. D. Wea Siga, K. Masumoto, M. Iwai, M. Fadil, M. S. Ahmad, J. K. Christopher Agutaya, Y. Inomata, A. T. Quitain, A. Hardiansyah, T. Kida, *ACS Appl. Mater. Interfaces* **2023**, *15*, 52724.

[7] Y. Shin, J. Chang, Y. Lee, T. Kang, *ACS Sens.* **2020**, *5*, 2221.

[8] a) C. Bai, J. Zhang, Y. Qin, Q. Meng, J. Yao, H. Huang, B. Wei, R. Li, L. Zhang, H. Miao, C. Qu, R. Qiao, *Anal. Chem.* **2022**, *94*, 11298; b) J. Morstein, D. Höfler, K. Ueno, J. W. Jurss, R. R. Walvoord, K. J. Bruemmer, S. P. Rezgui, T. F. Brewer, M. Saitoe, B. W. Michel, C. J. Chang, *J. Am. Chem. Soc.* **2020**, *142*, 15917.

[9] S. Huang, X. Liu, J. Hou, M. Liu, T. Luo, X. Huang, F. Chen, J. Dong, W. Zeng, *J. Mat. Chem. B.* **2023**, *11*, 3871.

[10] S. Xu, H. W. Liu, X. Yin, L. Yuan, S. Y. Huan, X. B. Zhang, *Chem. Sci.* **2019**, *10*, 320.

[11] K. Liu, X. Kong, Y. Ma, W. Lin, *Angew. Chem., Int. Ed.* **2017**, *56*, 13489.

[12] a) Y. Wu, D. Hu, D. Gao, C. Liu, H. Zheng, Z. Sheng, *Adv. Healthcare Mater.* **2022**, *11*, 2202379; b) T. Han, Y. Wang, S. Ma, M. Li, N. Zhu, S. Tao, J. Xu, B. Sun, Y. Jia, Y. Zhang, S. Zhu, B. Yang, *Adv. Sci.* **2022**, *9*, 2203474; c) X. Zhou, Q. Liu, W. Yuan, Z. Li, Y. Xu, W. Feng, C. Xu, F. Li, *Adv. Sci.* **2021**, *8*, 2000441; d) C. Chen, R. Tian, Y. Zeng, C. Chu, G. Liu, *Bioconjugate Chem.* **2020**, *31*, 276; e) Z. Chen, Z. Zhang, F. Zeng, S. Wu, *Chem. Biomed. Imaging* **2023**, *1*, 716; f) K. W. Lee, H. Chen, Y. Wan, Z. Zhang, Z. Huang, S. Li, C. S. Lee, *Biomaterials* **2022**, *289*, 121753.

[13] X. Zhang, S. Li, H. Ma, H. Wang, R. Zhang, X. D. Zhang, *Theranostics* **2022**, *12*, 3345.

[14] a) A. K. Mandal, X. Wu, J. S. Ferreira, M. Kim, L. R. Powell, H. Kwon, L. Groc, Y. H. Wang, L. Cognet, *Sci. Rep.* **2020**, *10*, 5286; b) T. Takeuchi, Y. Iizumi, M. Yudasaka, S. Kizaka-Kondoh, T. Okazaki, *Bioconjugate Chem.* **2019**, *30*, 1323.

[15] a) L. Wu, M. Jiang, C. Chu, T. Luo, Y. Hui, W. Zhou, S. Geng, X. F. Yu, *Adv. Sci.* **2024**, *11*, 2305762; b) B. Li, G. Wang, Y. Tong, Y. Zhang, S. K. Sun, C. Yu, *ACS Biomater. Sci. Eng.* **2023**, *9*, 449; c) M. Verma, Y. H. Chan, S. Saha, M. H. Liu, *ACS Appl. Bio Mater.* **2021**, *4*, 2142; d) L. L. Chen, Z. G. Wang, H. Zhang, L. M. Chen, L. Zhao, Z. Y. Liu, W. Zhao, L. H. Jiang, A. X. Ma, X. Yang, S. L. Liu, S. Zhang, D. W. Pang, *Chem. Biomed. Imaging* **2023**, *1*, 81.

[16] a) Q. Wang, Z. Zhang, D. Qiu, X. Mao, Z. Zhou, T. Xia, J. Wei, Q. Ding, X. Zhang, *Nanomaterials* **2022**, *12*, 4478; b) Y. Song, M. Lu, Y. Xie, G. Sun, J. Chen, H. Zhang, X. Liu, F. Zhang, L. Sun, *Adv. Funct. Mater.* **2022**, *32*, 2206802; c) L. Tong, J. Cao, K. Wang, J. Song, J. Mu, *Adv. Opt. Mater.* **2024**, *12*, 2301767; d) M. Zhao, A. Sik, H. Zhang, F. Zhang, *Adv. Opt. Mater.* **2023**, *11*, 2202039; e) P. Pei, Y. Chen, C. Sun,

Y. Fan, Y. Yang, X. Liu, L. Lu, M. Zhao, H. Zhang, D. Zhao, X. Liu, F. Zhang, *Nat. Nanotechnol.* **2021**, *16*, 1011.

[17] a) S. Zhu, R. Tian, A. L. Antaris, X. Chen, H. Dai, *Adv. Mater.* **2019**, *31*, 1900321; b) X. Sun, P. K. Chintakunta, A. A. Badachhape, R. Bhavane, H. J. Lee, D. S. Yang, Z. Starosolski, K. B. Ghaghada, P. G. Vekilov, A. V. Annapragada, E. A. Tanifum, *Adv. Sci.* **2023**, *10*, 2206435; c) Y. Su, B. Yu, S. Wang, H. Cong, Y. Shen, *Biomaterials* **2021**, *271*, 120717; d) Y. F. Ou, T. B. Ren, L. Yuan, X. B. Zhang, *Chem. Biomed. Imaging* **2023**, *1*, 220.

[18] a) Z. Tang, B. Song, H. Ma, T. Luo, L. Guo, J. Yuan, *Anal. Chem.* **2019**, *91*, 2939; b) M. Ye, Q. Tan, D. Jiang, J. Li, C. Yao, Y. Zhou, *ACS Appl. Mater. Interfaces* **2022**, *14*, 52659; c) J. Hong, Q. Xia, E. Zhou, G. Feng, *Talanta* **2020**, *215*, 120914.

[19] a) C. Wang, H. Lin, X. Ge, J. Mu, L. Su, X. Zhang, M. Niu, H. Yang, J. Song, *Adv. Funct. Mater.* **2021**, *31*, 2009942; b) Y. Han, J. An, M. Yuan, J. Fang, J. Zhang, L. Liang, Y. Liu, *Adv. Healthcare Mater.* **2024**, *13*, 2303845; c) P. Wu, Z. Qu, J. Zhang, X. Ren, D. Wang, C. Huang, K. Cheng, J. Qi, H. Shi, S. Gan, W. Wei, Y. Zhang, C. S. Lee, L. Wang, H. Sun, *Adv. Funct. Mater.* **2024**, *34*, 2400597.

[20] J. Xiang, C. Liu, L. Zhou, X. Yang, Y. Li, Y. Jiang, T. Mahmood, P. Zhang, P. Gong, L. Cai, *Anal. Chem.* **2020**, *92*, 4721.

[21] Y. Zhong, Z. Ma, S. Zhu, J. Yue, M. Zhang, A. L. Antaris, J. Yuan, R. Cui, H. Wan, Y. Zhou, W. Wang, N. F. Huang, J. Luo, Z. Hu, H. Dai, *Nat. Commun.* **2017**, *8*, 737.

[22] a) X. Zhang, W. Chen, X. Xie, Y. Li, D. Chen, Z. Chao, C. Liu, H. Ma, Y. Liu, H. Ju, *Angew. Chem., Int. Ed.* **2019**, *58*, 12117; b) Q. Wang, H. Yang, Y. Liu, Z. Zhou, X. Zhang, M. Sang, F. Xu, L. Song, T. Xia, Y. Zhang, J. Wei, X. Zhang, Q. Ding, *Adv. Healthcare Mater.* **2023**, *12*, 2300420.

[23] Z. Sun, H. Huang, R. Zhang, X. Yang, H. Yang, C. Li, Y. Zhang, Q. Wang, *Nano Lett.* **2021**, *21*, 6576.

[24] a) A. F. Tikum, W. Lim, M. M. Fortibui, S. Lee, S. Park, J. Kim, *Inorg. Chem.* **2021**, *60*, 7108; b) X. Fang, Y. Zhang, M. Li, Z. Zhang, Y. Qi, X. Zhang, X. Zhang, Y. Liu, J. Li, H. Yu, *Dyes Pigment.* **2023**, *209*, 110929.

[25] a) K. Ling, F. Men, W.-C. Wang, Y.-Q. Zhou, H.-W. Zhang, D.-W. Ye, *J. Med. Chem.* **2018**, *61*, 2611; b) H. Yan, J. Du, S. Zhu, G. Nie, H. Zhang, Z. Gu, Y. Zhao, *Small* **2019**, *15*, 1904382.

[26] R. Motterlini, J. E. Clark, R. Foresti, P. Sarathchandra, B. E. Mann, C. J. Green, *Circ. Res.* **2002**, *90*, 17.

[27] N. Wang, Z. Li, W. Liu, T. Deng, J. Yang, R. Yang, J. Li, *ACS Appl. Mater. Interfaces* **2019**, *11*, 26684.

[28] Y. Luo, Y. Lei, H. Zhou, Y. Chen, H. Liu, J. Jiang, C. Xu, B. Wu, *Cell Biol. Toxicol.* **2024**, *40*, 1.

[29] M. Yang, J. Fan, J. Du, X. Peng, *Chem. Sci.* **2020**, *11*, 5127.